Editors' Suggestion

Correlated Insulating States and Transport Signature of Superconductivity in Twisted Trilayer Graphene Superlattices

Xi Zhang,[1,*] Kan-Ting Tsai,[1,*] Ziyan Zhu,[2] Wei Ren,[1] Yujie Luo,[3] Stephen Carr,[2] Mitchell Luskin,[4] Efthimios Kaxiras,[2,5] and Ke Wang[1,†]

[1]School of Physics and Astronomy, University of Minnesota, Minneapolis, Minnesota 55455, USA
[2]Department of Physics, Harvard University, Cambridge, Massachusetts 02138, USA
[3]Department of Mechanical Engineering, University of Minnesota, Minneapolis, Minnesota 55455, USA
[4]School of Mathematics, University of Minnesota, Minneapolis, Minnesota 55455, USA
[5]John A. Paulson School of Engineering and Applied Sciences, Harvard University, Cambridge, Massachusetts 02138, USA

(Received 2 November 2020; accepted 3 September 2021; published 11 October 2021)

Layers of two-dimensional materials stacked with a small twist angle give rise to beating periodic patterns on a scale much larger than the original lattice, referred to as a "moiré superlattice." Here, we demonstrate a higher-order "moiré of moiré" superlattice in twisted trilayer graphene with two consecutive small twist angles. We report correlated insulating states near the half filling of the moiré of moiré superlattice at an extremely low carrier density ($\sim 10^{10}$ cm^{-2}), near which we also report a zero-resistance transport behavior typically expected in a 2D superconductor. The full-occupancy ($\nu = -4$ and $\nu = 4$) states are semimetallic and gapless, distinct from the twisted bilayer systems.

DOI: 10.1103/PhysRevLett.127.166802

When two layers of van der Waals (vdW) materials are placed on top of each other with a twist angle, isolated flat bands may emerge near the zero energy [1,2], giving rise to unconventional correlated phases including Mott insulator [3–5] and superconductivity [6]. This discovery sparked extensive theoretical [7–13] and experimental investigations [14–16] into its microscopic mechanism, and recent efforts have been geared toward extensions to other material combinations [17], including higher-order moiré systems consisting of multiple twisted pieces of vdW materials [18–21].

In this work, we fabricate a novel twisted trilayer graphene (tTLG) system with two independently controlled twist angles, in which three pieces of monolayer graphene are transferred on top of each other with designed twist angles in the range of 2°–3° [Fig. 1(a)] between adjacent layers. The full trilayer stack is encapsulated in hexagonal boron nitride (hBN), and bubble-free regions of a few microns in size are identified. The sample is then etched down to 3 μm × 3 μm size with a 1D edge contact [22] defined at each corner [Fig. 1(a)], allowing four-probe transport measurements. In this platform, a "moiré of moiré" (MoM) superlattice [1] forms due to the interference of two sets of misaligned twisted bilayer superlattices between the 1-2 and 2-3 layer pairs [Fig. 1(b)]. AFM topography of tTLG made at a consecutive twist angle of 1.64° [Fig. 1(a)] demonstrates the MoM, following previously established methods [16,23]. Enhancement of the electronic density of states (DOS) occurs for a wide range of twist angles, at which the electron correlation may become important, making tTLG a unique platform to explore correlated states with more versatile experimental control. In this work, we report controlled experimental studies of two MoM lattices (defined in the following as MoM 1 and MoM 2), with unit cell sizes extracted to be $A_1 = 6438$ nm^2 and $A_2 = 4778$ nm^2, respectively [24]. In contrast to the moiré superlattice in twisted bilayer graphene (tBLG), a given unit cell size of MoM lattice in tTLG can correspond to a range of different possible twist-angle combinations; that is, the MoM length scale is not a unique function of the two twist angles. Figure 1(c) shows all possible twist-angle combinations for MoM 1 with color scale representing the DOS maximum, with 1D cuts plotted in Fig. 1(d), corresponding to the scattered points in Fig. 1(c). The DOS exhibits a large value, comparable to tBLG, for a range of twist-angle configurations. In these regions, the electronic band structure is characterized by flat bands at the charge-neutrality point (CNP) despite the lack of a band gap [Figs. 1(e)–1(g)], signaling enhanced electronic correlation. The twist angles that exhibit flat bands [Figs. 1(c) and 1(d)] agree with the possible twist angles of the experimental devices considering layer migration and twist-angle inhomogeneity [24].

In Fig. 2(a), we show the measured resistance R of MoM 1 as a function of the temperature spanning the entire range of band occupancy on the electron and hole sides. To describe the band occupancy, in the following, we use the definition of "filling factor" $\nu = n/(n_s/4)$, where n is the carrier density controlled by the silicon back gate and n_s is the carrier density corresponding to four charge carriers per MoM unit cell (full occupancy). Resistance peaks are observed at all even fillings, similar to twisted-bilayer

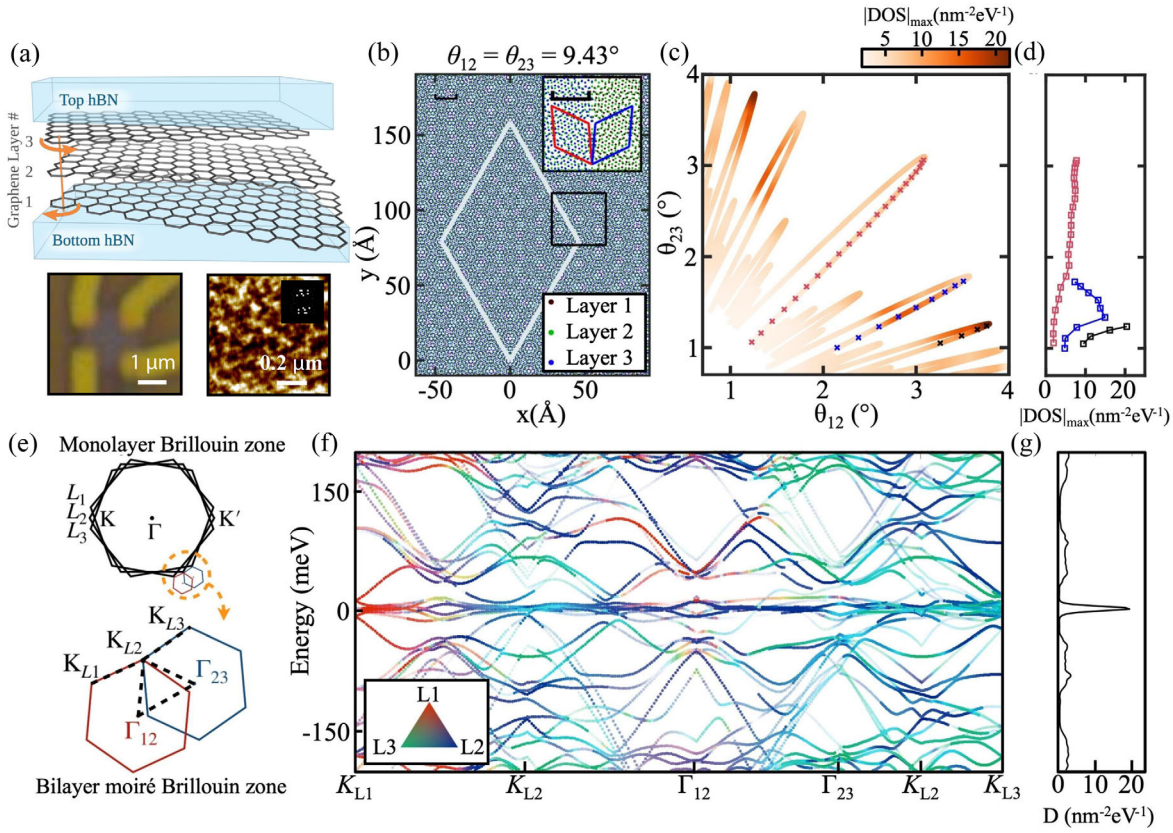

FIG. 1. MoM superlattices in tTLG. (a) Schematic of the hBN-encapsulated tTLG device, consisting of three-monolayer graphene consecutively twisted with respect to the previous layer. Bottom left: optical microscope image of a typical device under study. Bottom right: AFM topology of tTLG on hBN, made at consecutive twist angles of 1.64° for demonstration of tTLG MoM. Irregular and triangularlike patterns with a length scale on the order of 300 nm are barely visible, suggesting a plethora of coexisting MoM length scales accompanying the dominating MoM lattice. Inset: dominating Fourier components in the FFT spectrum, corresponding to length scales of 120–260 nm, which qualitatively agrees with experimental design. (b) Atomic positions in tTLG at a set of commensurate angles $\theta_{12} = \theta_{23} = 9.43°$ demonstrating the MoM superlattice. White parallelogram: MoM supercell. Inset: enlargement of the area inside the black box showing the bilayer moiré pattern. The left (right) shows only layers 2 and 1 (3), and the red (blue) parallelograms show the corresponding bilayer moiré supercells. Both scale bars are 10 Å. (c) Possible twist-angle combinations for MoM area $A_1 = 6438$ nm^2 (MOM 1). Color scale represents the density of state maximum. (d) 1D cuts along twist-angle configurations near $\theta_{12} = \theta_{23}$, $\theta_{12} = 2\theta_{23}$, and $\theta_{12} = 3\theta_{23}$, respectively. (e) Monolayer Brillouin zone of the three individual layers (top) and the bilayer moiré Brillouin zone formed between adjacent bilayer pairs (bottom). (f) Band structure at $\theta_{12} = 2.9°$ and $\theta_{23} = 1.4°$ along the high symmetry line indicated by the dashed line in (e). Colors indicate the projected weight onto the state at the center momentum in each layer. Red, layer 1; blue, layer 2; green, layer 3. (g) Normalized density of states corresponding to band structure shown in (f), with a zero-energy peak value comparable to that of tBLG.

systems but comparably much lower in amplitude. Conductance differences on and off even-filling peaks are orders of magnitude larger than what can be expected from universal mesoscopic noise and the characterized system noise [24]. To demonstrate the temperature dependence of each filling, we plot the measured conductance as a function of the carrier density at different temperatures [Fig. 2(c)] and as a function of the temperature at each signature filling factor [Fig. 2(e)]. We also present a control study of MoM 2 [Figs. 2(b), 2(d), and 2(f)]. Here, $n_s = 6.22 \times 10^{10}$ cm^{-2} (8.37×10^{10} cm^{-2}) is extracted from the resistance peak positions for MoM 1 (MoM 2). While the local twist angle can change within the same stack, our transport data for each device show well-defined and uniformly separated resistance peaks, at the carrier density corresponding to a single moiré of moiré lattice that is consistent with our theoretical expectation and experimental twist-angle target. This suggests that the transport signature of each device is dominated by (or primarily comes from) a single well-defined moiré of moiré lattice. At $\nu = -4$ and $\nu = 4$, the measured resistance is similar to that of the charge neutrality point ($\nu = 0$) and displays little or no temperature dependence at full-occupancy states due to the absence of a band gap, distinct from the previously reported highly insulating gap at full occupancy in moiré bilayer systems [3,6,38–40]. This observation is consistent with our electronic structure result that tTLG is gapless and provides the first experimental evidence that correlated

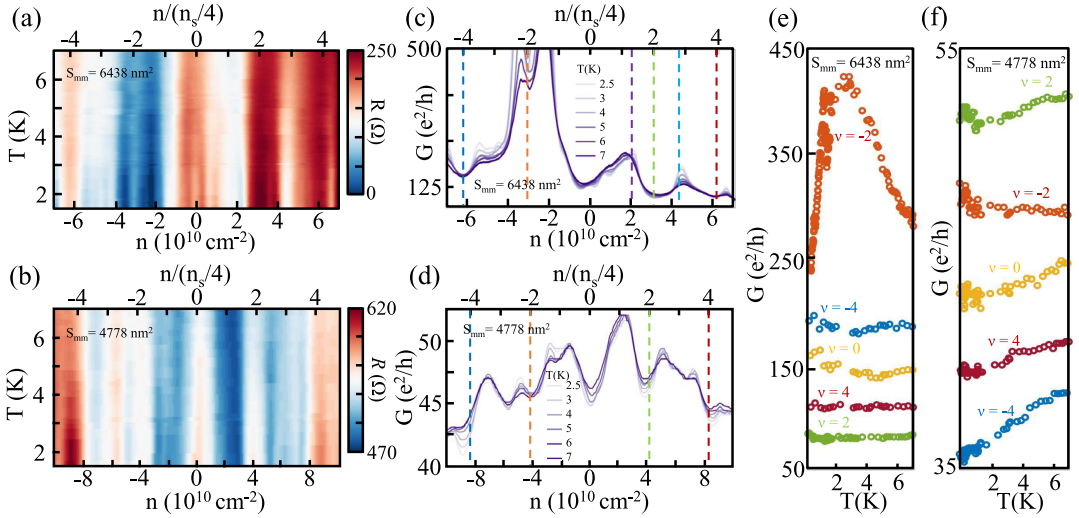

FIG. 2. Insulating and semimetallic behavior at $\nu =$ even integer fillings of two MoM superlattices. (a) Measured four-probe resistance of MoM 1 (unit cell size $= 6438$ nm^2) and (b) MoM 2 (unit cell size $A_2 = 4778$ nm^2) as a function of the temperature and carrier density n. Resistance peaks are observed at all $\nu = n/(n_s/4) =$ even integer fillings, where n_s is the carrier density corresponding to four charge carriers per MoM unit cell. (c) Line traces of four-probe conductance as a function of the carrier density taken at different temperatures of MoM 1 and (d) MoM 2. (e) Conductance as a function of the temperature at each even filling for MoM 1 and (f) MoM 2. Data are offset to separate each curve.

transport behavior can arise from nonisolated flat electronic bands.

In contrast to the semimetallic behavior of the states at full occupancy, the states at half filling for MoM 1 exhibit an insulatorlike temperature dependence [Fig. 2(c)], with a rough estimation of the activation gap of 0.168 meV at $\nu = -2$ [24], which is qualitatively consistent with the observed metal-insulator transition near ~3 K. The definition of an insulator here is in the context of the temperature dependence only, as the absolute value of the measured resistance at half filling is, in fact, lower than that of semimetallic full-occupancy and zero-occupancy states. Around $\nu = -2$, the measured resistance is observed to be zero below ~3 K. The zero-resistance states are particle-hole asymmetric. Two zero-resistance domes are observed (corresponding to Fig. 3) near $\nu = -2$, while two nonzero resistance dips are found near $\nu = 2$ filling [24] (labeled as $\nu = 2^-$ and $\nu = 2^+$), as well as at both half-filling states of MoM 2 with strong metallic temperature dependence (Fig. 2). The widths of all resistance peaks including the CNP in each case are on the order of 10^{10} cm^{-2}, suggesting state-of-the-art device quality necessary for resolving the MoM correlated states.

The low carrier density of these resistance peaks corresponds to the filling of the tTLG MoM supercell (instead of the bilayer moiré supercells from either the 1-2 or 2-3 layer pair), which is 2 orders of magnitude larger in area [24] compared to the previously reported tBLG moiré supercell. The corresponding possible angle configurations [Fig. 1(c)] are consistent with our experimentally targeted value, considering unavoidable layer migration during the assembly process [41].

Because of the incommensurate nature of tTLG MoM superlattice, the small local twist-angle inhomogeneity between twisted graphene interfaces [40,42] can also result in larger spatial variation in the MoM unit cell area, making the observation of MoM correlated states extremely challenging. In MoM 2, which is found a few microns away on the same tTLG stack as MoM 1, the metalliclike states are observed near half filling but do not evolve into zero-resistance states. Our observation is similar to the magic-angle continuum previously reported [17], where superconductinglike states are extremely sensitive to a slight change in twist angle while correlated insulator states are more robust.

In Fig. 3(a), we show the measured four-probe resistance near $\nu = -2$ for MoM 1 at zero magnetic field, as a function of the carrier density and temperature. At a carrier density around 3.11×10^{10} cm^{-2}, the resistance first decreases (metal-like) from 20 to 4 K and then increases (insulatorlike) from 4 K down to 10 mK. We identify this change in behavior at 4 K as a correlated insulator state corresponding to half filling, similar to that in tBLG [6,38]. Two zero-resistance domes are also found on either side of the half-filling insulating state below the same critical temperature, $T_c \sim 4$ K, which implies that correlated phases emerge below this critical temperature in our device. The span of the zero-resistance domes, as well as the carrier density at which each state was found, is about 2 orders of magnitude smaller than those in all the previously reported twisted-bilayer systems. We show [Figs. 3(b)and 3(c)] the four-probe differential resistance as a function of the temperature and as a function of the carrier density and applied dc bias at $T = 3$ K. A broad temperature transition

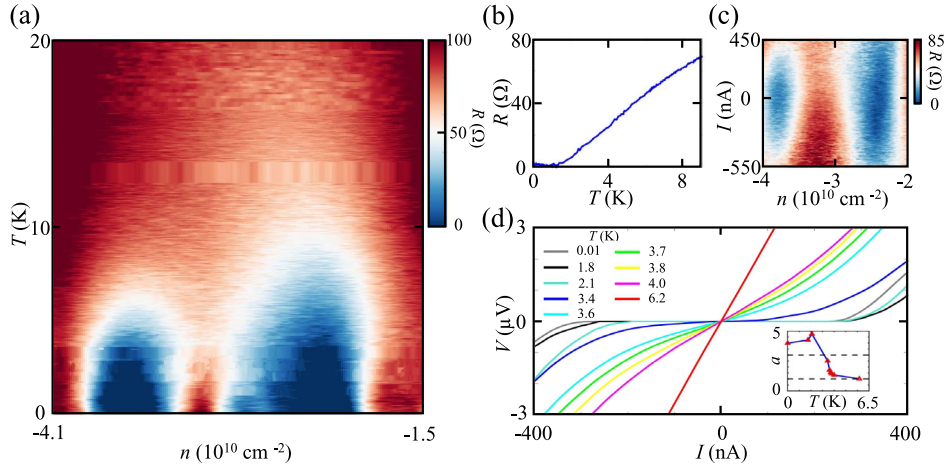

FIG. 3. Temperature and bias characteristics of superconductinglike states. (a) Measured four-probe resistance of MoM 1 as a function of the carrier density and temperature. At half filling of the MoM superlattice ($n \sim -3.22 \times 10^{10}$ cm^{-2}), correlated insulating behavior is observed with two adjacent zero-resistance domes. (b) Differential resistance as a function of the temperature near the center of the right zero-resistance dome. (c) Differential resistance as a function of the carrier density and dc bias offset at 3 K. Zero-resistance states symmetric with respect to zero bias exist up to $J_c \sim 200$ nA. (d) I-V characteristics at different temperatures, near the center of the right zero-resistance dome. The I-V curve power law exponent goes from 1 to 3 as the temperature decreases, consistent with the BKT model for a typical 2D superconductor. Inset: the temperature dependence of the power law exponent α, from which a critical temperature $T_{\mathrm{BKT}} \sim 3.4$ K is extracted.

was observed, similar to previously reported twisted transition metal dichalcogenides [17] and twisted double bilayer graphene [39] systems, making it unreliable to determine critical temperature from the $R(T)$ curve alone. Zero-resistance states exist in two domes symmetrically with respect to the zero bias, which is typically expected from a 2D superconductor. The critical current J_c of the zero-resistance state at the higher doping is also visibly smaller, consistent with the observation in Fig. 2(a). The I-V characteristics imply a critical current $J_c \sim 200$ nA at 3 K. As the temperature increases above T_c, the I-V characteristics [Fig. 3(d)] evolve from cubic dependence (superconductinglike) to linear dependence (metal), consistent with the Berezinskii-Kosterlitz-Thouless (BKT) model of 2D superconductivity [43]. The power law of each I-V curve taken at different temperatures indicates a BKT transition temperature of $T_{\mathrm{BKT}} \sim 3.4$ K [Fig. 3(d), inset]. The reported transport signatures [Figs. 3(a)–3(d)] represent typical behavior expected from a 2D superconductor, similar to previously reported tBLG following the same well-developed experimental protocol. The observed width of the transitions (in temperature and I-V) are also consistent with a spatially varying superconducting order due to angle inhomogeneity [24].

However, additional experiments are needed in order to provide independent evidence for phase coherence (i.e., via gate-defined Josephson junctions), to assertively confirm the superconducting nature of the observed zero-resistance states. Previous studies on tBLG show that critical current exhibits a weak oscillatory dependence [6] on the value of the in-plane magnetic field, as a result of accidental Josephson junction formation between coexisting superconducting ($\nu = 2$) and insulating ($\nu = 4$) domains due to twist-angle inhomogeneity. However, the $\nu = 4$ full-occupancy state in tTLG is semimetallic, and the moiré of moiré is more sensitive to angle inhomogeneity due to involvement of two twist angles and a plethora of underlying length scales. Therefore, an accidental Josephson junction with a sufficiently weak link may be more difficult to form in tTLG. Future demonstration of a similar "Fraunhofer pattern" in tTLG, therefore, may require a tTLG-hBN-tTLG vertical tunnel junction, which is beyond the scope of the present work.

Magnetotransport studies are commonly used to characterize moiré length scales. The MoM pattern is incommensurate by nature and a continuum of length scales coexists, resulting in a plethora of complicated magnetotransport behavior that cannot be traced back to a definitive origin. To demonstrate these major differences from tBLG, we show magnetotransport data for the tTLG MoM 1 system (Fig. 4). The amplitude of transport features are $\sim 10^5$ larger than the mesoscopic and system noise [43]. The distances between each fan at even integer fillings are as narrow as $\sim 10^{10}$ cm^{-2}, already comparable to the state-of-the-art disorder broadening [44], thus exhibiting several sets of nearly overlapping Hofstadter butterfly patterns [45]. A twofold degeneracy of Landau levels is observed, consistent with valley-symmetry breaking in our band calculation [24]. In addition to the experimentally limited resolution of 10^{10} cm^{-2}, the indistinguishable Landau fans are also a signature of the tTLG systems due to their incommensurate nature even in the continuum limit. In

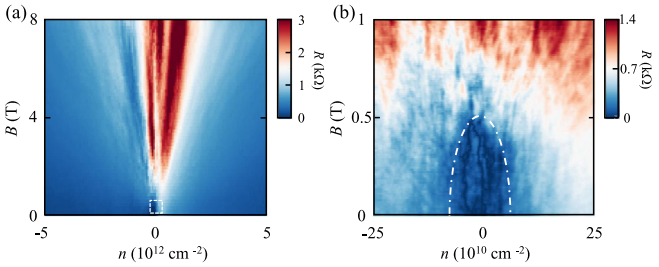

FIG. 4. Magnetotransport at larger carrier density span. (a) Resistance of MoM 1 as a function of the magnetic field and a large range of carrier density. Zero-resistance states are observed only in a very small density range near zero carrier density. (b) Magnetotransport data in a smaller range of carrier density, displaying a very complicated Hofstadter butterfly pattern, in which zero-resistance states exist up to ∼500 mT.

twisted bilayer systems, there always exists a dominant moiré length corresponding to the same repeating motif. In contrast, in tTLG, the interference between the two different misaligned bilayer moiré patterns can result in multiple MoM harmonics with comparable length scales at certain twist angles, leading to the lack of an apparent repeating pattern [24]. Moreover, in tTLG, a small continuous change in the twist angles does not necessarily correspond to a smooth change in the length scale, and the resulting MoM supercell area can be drastically different [24]. Despite the complications, a zero-resistance dome can be identified [Fig. 4(b)] up to ∼500 mT, though its superconducting nature requires future experimental studies to verify.

In conclusion, we have constructed a MoM superlattice in a novel twisted trilayer graphene architecture. The electronic band structure consists of a nonisolated zero-energy flat band, which we experimentally confirmed with observed semimetallic resistance peaks at full occupancy of the MoM supercell. Despite this major difference, correlated insulating states are found at half filling, near which we also report zero-resistance states at an unprecedented low carrier density and a comparably high critical temperature of $T_{\mathrm{BKT}} \sim 3.4$ K, which are tentatively attributed to superconductivity, though future work providing further experimental evidence for macroscopic coherence will be needed. This demonstrates that an isolated flat band may not be required for the emergence of moiré correlated behaviors. While further experimental and theoretical studies on this new material platform are necessary to confirm the existence of superconductivity, our system exhibits both some similarities with the phase diagram in tBLG and transport properties distinct from tBLG, which shed new light on the microscopic origin of moiré correlated states.

We thank Philip Kim, Allen Goldman, Paul Crowell, and Hyobin Yoo for helpful experimental discussions and Andrey Chubukov, Rafael Fernandes, and Boris Shklovski for helpful theoretical discussion. Electrical transport study is supported by ARO MURI Grant No. W911NF-14-1-0247. Structural study is supported by NSF DMREF Grant No. 1922165. Z. Z. and S. C. are supported by the STC Center for Integrated Quantum Materials, NSF Grant No. DMR-1231319. Portions of this work were conducted in the Minnesota Nano Center, which is supported by the National Science Foundation through the National Nanotechnology Coordinated Infrastructure (NNCI) under Award No. ECCS-2025124.

*These authors contributed equally to this work.
†kewang@umn.edu

[1] R. Bistritzer and A. H. MacDonald, Proc. Natl. Acad. Sci. U.S.A. **108**, 12233 (2011).
[2] G. Tarnopolsky, A. J. Kruchkov, and A. Vishwanath, Phys. Rev. Lett. **122**, 106405 (2019).
[3] Y. Cao, V. Fatemi, A. Demir, S. Fang, S. L. Tomarken, J. Y. Luo, J. D. Sanchez-Yamagishi, K. Watanabe, T. Taniguchi, E. Kaxiras, R. C. Ashoori, and P. Jarillo-Herrero, Nature (London) **556**, 80 (2018).
[4] G. Chen, L. Jiang, S. Wu, B. Lyu, H. Li, B. L. Chittari, K. Watanabe, T. Taniguchi, Z. Shi, J. Jung, Y. Zhang, and F. Wang, Nat. Phys. **15**, 237 (2019).
[5] Y. Xie, B. Lian, B. Jäck, X. Liu, C.-L. Chiu, K. Watanabe, T. Taniguchi, B. A. Bernevig, and A. Yazdani, Nature (London) **572**, 101 (2019).
[6] Y. Cao, V. Fatemi, S. Fang, K. Watanabe, T. Taniguchi, E. Kaxiras, and P. Jarillo-Herrero, Nature (London) **556**, 43 (2018).
[7] H. C. Po, L. Zou, A. Vishwanath, and T. Senthil, Phys. Rev. X **8**, 031089 (2018).
[8] H. Isobe, N. F. Q. Yuan, and L. Fu, Phys. Rev. X **8**, 041041 (2018).
[9] F. Wu, A. H. MacDonald, and I. Martin, Phys. Rev. Lett. **121**, 257001 (2018).
[10] S. Carr, S. Fang, Z. Zhu, and E. Kaxiras, Phys. Rev. Research **1**, 013001 (2019).
[11] J. F. Dodaro, S. A. Kivelson, Y. Schattner, X. Q. Sun, and C. Wang, Phys. Rev. B **98**, 075154 (2018).
[12] S. Carr, S. Fang, H. C. Po, A. Vishwanath, and E. Kaxiras, Phys. Rev. Research **1**, 033072 (2019).
[13] M. Le Ster, T. Märkl, and S. A. Brown, 2D Mater. **7**, 011005 (2019).
[14] H. Polshyn, M. Yankowitz, S. Chen, Y. Zhang, K. Watanabe, T. Taniguchi, C. R. Dean, and A. F. Young, Nat. Phys. **15**, 1011 (2019).
[15] N. R. Finney, M. Yankowitz, L. Muraleetharan, K. Watanabe, T. Taniguchi, C. R. Dean, and J. Hone, Nat. Nanotechnol. **14**, 1029 (2019).
[16] Z. Wang *et al.*, Sci. Adv. **5**, eaay8897 (2019).
[17] L. Wang, E.-M. Shih, A. Ghiotto, L. Xian, D. A. Rhodes, C. Tan, M. Claassen, D. M. Kennes, Y. Bai, B. Kim, K. Watanabe, T. Taniguchi, X. Zhu, J. Hone, A. Rubio, A. N. Pasupathy, and C. R. Dean, Nat. Mater. **19**, 861 (2020).
[18] Z. Zhu, P. Cazeaux, M. Luskin, and E. Kaxiras, Phys. Rev. B **101**, 224107 (2020).

[19] C. Mora, N. Regnault, and B. A. Bernevig, Phys. Rev. Lett. **123**, 026402 (2019).
[20] B. Amorim and E. V. Castro, arXiv:1807.11909.
[21] S. Carr, C. Li, Z. Zhu, E. Kaxiras, S. Sachdev, and A. Kruchkov, Nano Lett. **20**, 3030 (2020).
[22] L. Wang, I. Meric, P. Y. Huang, Q. Gao, Y. Gao, H. Tran, T. Taniguchi, K. Watanabe, L. M. Campos, D. A. Muller, J. Guo, P. Kim, J. Hone, K. L. Shepard, and C. R. Dean, Science **342**, 614 (2013).
[23] L. Wang, S. Zihlmann, M.-H. Liu, P. Makk, K. Watanabe, T. Taniguchi, A. Baumgartner, and C. Schönenberger, Nano Lett. **19**, 2371 (2019).
[24] See Supplemental Material at http://link.aps.org/supplemental/10.1103/PhysRevLett.127.166802 for more details, which includes Refs. [25–37].
[25] A. K. Geim, Science **324**, 1530 (2009).
[26] C. R. Dean, A. F. Young, I. Meric, C. Lee, L. Wang, S. Sorgenfrei, K. Watanabe, T. Taniguchi, P. Kim, K. L. Shepard, and J. Hone, Nat. Nanotechnol. **5**, 722 (2010).
[27] S. Fang and E. Kaxiras, Phys. Rev. B **93**, 235153 (2016).
[28] Z. Zhu, S. Carr, D. Massatt, M. Luskin, and E. Kaxiras, Phys. Rev. Lett. **125**, 116404 (2020).
[29] J. M. Pomeroy and H. Grube, J. Appl. Phys. **105**, 094503 (2009).
[30] J. I. A. Li, C. Tan, S. Chen, Y. Zeng, T. Taniguchi, K. Watanabe, J. Hone, and C. R. Dean, Science **358**, 648 (2017).
[31] S. Wu, V. Fatemi, Q. D. Gibson, K. Watanabe, T. Taniguchi, R. J. Cava, and P. Jarillo-Herrero, Science **359**, 76 (2018).
[32] J. Robertson, Eur. Phys. J. Appl. Phys. **28**, 265 (2004).
[33] A. Laturia, M. L. Van de Put, and W. G. Vandenberghe, npj 2D Mater. Appl. **2**, 6 (2018).
[34] P. A. Lee and A. D. Stone, Phys. Rev. Lett. **55**, 1622 (1985).
[35] J. Berezovsky, M. F. Borunda, E. J. Heller, and R. M. Westervelt, Nanotechnology **21**, 274013 (2010).
[36] K. R. Amin, S. S. Ray, N. Pal, R. Pandit, and A. Bid, Commun. Phys. **1**, 1 (2018).
[37] V. Zdravkov, A. Sidorenko, G. Obermeier, S. Gsell, M. Schreck, C. Müller, S. Horn, R. Tidecks, and L. R. Tagirov, Phys. Rev. Lett. **97**, 057004 (2006).
[38] X. Lu, P. Stepanov, W. Yang, M. Xie, M. A. Aamir, I. Das, C. Urgell, K. Watanabe, T. Taniguchi, G. Zhang, A. Bachtold, A. H. MacDonald, and D. K. Efetov, Nature (London) **574**, 653 (2019).
[39] X. Liu, Z. Hao, E. Khalaf, J. Y. Lee, Y. Ronen, H. Yoo, D. Haei Najafabadi, K. Watanabe, T. Taniguchi, A. Vishwanath, and P. Kim, Nature (London) **583**, 221 (2020).
[40] Y. Cao, D. Rodan-Legrain, O. Rubies-Bigorda, J. M. Park, K. Watanabe, T. Taniguchi, and P. Jarillo-Herrero, Nature (London) **583**, 215 (2020).
[41] M. Yankowitz, S. Chen, H. Polshyn, Y. Zhang, K. Watanabe, T. Taniguchi, D. Graf, A. F. Young, and C. R. Dean, Science **363**, 1059 (2019).
[42] A. Uri, S. Grover, Y. Cao, J. A. Crosse, K. Bagani, D. Rodan-Legrain, Y. Myasoedov, K. Watanabe, T. Taniguchi, P. Moon, M. Koshino, P. Jarillo-Herrero, and E. Zeldov, Nature (London) **581**, 47 (2020).
[43] J. M. Kosterlitz and D. J. Thouless, J. Phys. C **6**, 1181 (1973).
[44] C. R. Dean, L. Wang, P. Maher, C. Forsythe, F. Ghahari, Y. Gao, J. Katoch, M. Ishigami, P. Moon, M. Koshino, T. Taniguchi, K. Watanabe, K. L. Shepard, J. Hone, and P. Kim, Nature (London) **497**, 598 (2013).
[45] B. Hunt, J. D. Sanchez-Yamagishi, A. F. Young, M. Yankowitz, B. J. LeRoy, K. Watanabe, T. Taniguchi, P. Moon, M. Koshino, P. Jarillo-Herrero, and R. C. Ashoori, Science **340**, 1427 (2013).